Rev. Roum. Sci. Techn.– Électrotechn. et Énerg.
Vol. **71**, *3*, pp. 367–372, Bucarest, 2026

# REAL-TIME ASSESSMENT OF A SOLAR WATER PUMPING SYSTEM UNDER NORMAL AND FAULTY OPERATING CONDITIONS

NORA REZAIGUIA[1], OUALID AISSA[1], HICHAM TALHAOUI[1], ABDELBASSET KRAMA[2], ABDELHALIM KESSAL[1], ABDERRAHIM REFFAS[1]

**Keywords: Irrigation system; Solar energy; Adaptive neuro-fuzzy inference system – maximum power point tracking (ANFIS-MPPT); Healthy and faulty induction motor; Hardware-in-the-loop (HIL) tests.**

**Solar-powered water-pumping systems are indispensable for ensuring consistent, efficient crop irrigation in remote, off-grid regions. In this paper, an advanced control strategy is implemented using the adaptive neuro-fuzzy inference system (ANFIS) to ensure maximum power extraction under all weather conditions. In addition, the induction motor (whether healthy or with one or more broken rotor bars) is coupled to a centrifugal pump in the solar water pumping system (SWPS). The motor's performance is precisely controlled using direct torque control (DTC). Furthermore, a fast Fourier transform (FFT) is used to monitor the induction motor's state in the SWPS. Finally, the developed SWPS, operating under both healthy and faulty conditions, is experimentally validated via hardware-in-the-loop (HIL) tests using the OPAL-RT OP5600 platform and the Virtex-6 ML605 FPGA. Thanks to the applied methods, the investigated SWPS exhibits highly satisfactory, reliable performance across varying operating conditions.**

## 1. INTRODUCTION

Renewable energy has emerged as a vital component in the pursuit of sustainability and progress, serving as the foundation for a more environmentally and economically sustainable future [1,2]. This clean, renewable energy is a key factor in facilitating the transition to a greener, more financially stable global energy landscape [3]. Considering these changes, nonlinear solar water pumping systems (SWPS$_s$) have emerged as a leading technological solution with a significant impact on the agricultural sector [2–5]. These systems are especially beneficial in remote areas with limited access to traditional electricity grids. Two fundamental components define the SWPS: the photovoltaic (PV) power supply, integrated with a strategy for maximizing power output, and the regulated electric motor that drives the water pump efficiently [6-8]. Maximum power point tracking (MPPT) is not only an essential mechanism for optimizing the power output of the PV panel but also determines the reference speeds [5]. Over the past few decades, several techniques have been proposed and have demonstrated impressive capabilities in tracking the MPP and exhibiting rapid convergence in response to environmental changes, playing a significant role in the relevant literature [9–11]. Artificial Intelligence (AI) approaches have been suggested to address the shortcomings of traditional algorithms, such as perturb and observe (P&O) and incremental conductance (INC) [12,13]. These intelligent approaches, largely based on fuzzy logic theory and artificial neural networks, offer the advantage of not requiring exact parameters or complex mathematical modeling of the systems under study [14–16].

The adaptive neuro-fuzzy inference system (ANFIS) represents a significant advancement in the field of artificial intelligence, integrating the learning capabilities of neural networks with the flexibility of fuzzy logic. This synergy enhances both technologies, resulting in a more robust and powerful model, particularly in contexts where the relationships between variables are complex, non-linear, or imprecise [11,17,18]. For these reasons, the ANFIS-MPPT strategy is designed to manage complex data and respond to environmental changes, such as radiation and temperature variations, which are difficult to predict [12,19].

The induction motor (IM) is used due to its simple construction and operation [20,21]. However, various faults such as stator short circuits or the breakage of one or more rotor bars can affect the motor. Over time, these problems can lead to technical defects. These can cause the machine to fail and reduce its service life [22]. The aim of fault diagnosis is therefore to detect and locate issues within the motor, enabling early corrective actions that improve its performance and extend its operational lifespan [23]. On the other hand, the nonlinear nature of the IM makes control challenging, prompting researchers to develop various strategies to manage its behavior. Among the control strategies existing in the literature, direct torque control (DTC) is the most suitable approach for this type of motor. This is supported by the benefits offered by DTC, including its simple control structure and its ability to deliver excellent dynamic torque response [8,18,21].

This paper proposes a solar-powered water-pumping system that uses a water storage tank to irrigate a variety of agricultural crops. An effective control strategy is implemented, employing the ANFIS-MPPT method to ensure optimal power extraction under all weather conditions. Likewise, both the healthy and faulty IMs, caused by the breakage of one or more rotor bars, are integrated with the centrifugal pump in the solar-powered pumping system. The motor's operation is precisely regulated using the DTC method. A simple and effective technique, called the fast Fourier transform (FFT), is carried out in this paper for monitoring in a closed loop the state of the IM in the SWPS. By analyzing the stator current of the induction motor, faults can be easily detected. Finally, the developed SWPS was validated in both healthy and faulty modes using hardware-in-the-loop (HIL) tests on the OPAL-RT OP5600 platform and Virtex 6 ML605 FPGA, under different irradiance conditions. The results were robust and very satisfactory.

This paper is divided into seven sections. Following the introduction, Section 2 provides a comprehensive description of the developed SWPS. Section 3 explains the

[1]LPMRN Laboratory, Department of Electromechanical, Faculty of Sciences and Technology, University Mohamed El Bachir El Ibrahimi of Bordj Bou Arreridj, El-Anasser 34030, Algeria.
[2]Qatar Environment and Energy Research Institute, Hamad Bin Khalifa University, Doha, 34110, Qatar.
E-mails: nora.rezaiguia@univ-bba.dz, oualid.aissa@univ-bba.dz, hichem.talhaoui@univ-bba.dz, akrama@hbku.edu.qa, abdelhalim.kessal@univ-bba.dz, abderrahime.reffas@univ-bba.dz

DOI: 10.59277/RRST-EE.2026.3.5

MPPT's working principle using the ANFIS strategy. Section 4 focuses on the dynamic model of the IM, which is designed to facilitate analysis of rotor bar breakage faults. Section 5 presents the conventional DTC approach and outlines the key equations and specifications of the centrifugal pump employed in the studied SWPS. Section 6 exhibits the experimental findings, incorporating the FFT technique for the detection of broken rotor bars. Finally, Section 7 concludes the paper.

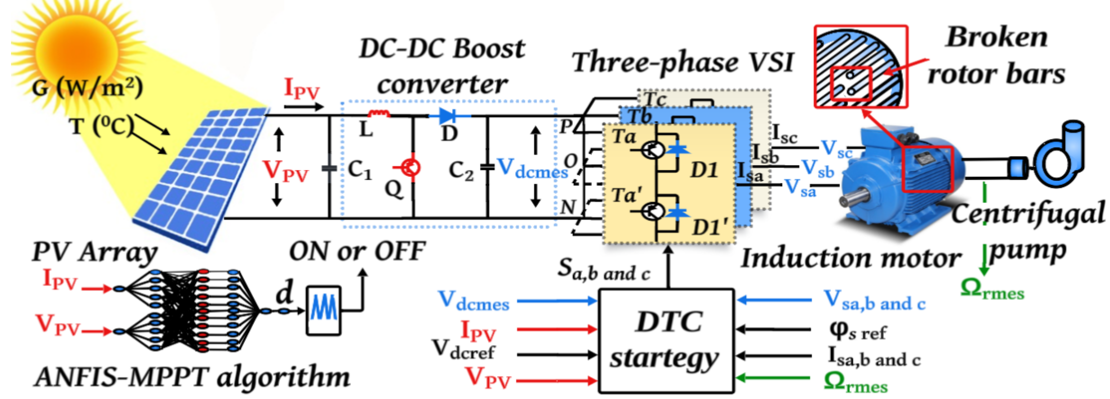


Fig. 1 – Detailed schematic depicting the operation of a faulty induction motor in the SWPS.

## 2. DESCRIPTION OF THE INVESTIGATED SWPS

The SWPS investigated in this study consists of two main power conversion stages, as illustrated in Fig. 1. The first stage involves a step-up DC-DC converter that boosts the voltage output from the PV array to a suitable level, using an intelligent ANFIS-based MPPT strategy. The second stage includes a DC-AC inverter that converts the regulated DC voltage into AC power to drive the induction motor, controlled via the DTC method. This motor, whether operating under healthy or faulty conditions, is mechanically coupled to a centrifugal pump that extracts water from the source and transfers it to a storage tank. The stored water is then used for irrigating various agricultural crops.

## 3. ADVANCED ANFIS-MPPT STRATEGY

In the field of control engineering and intelligent systems, the ANFIS algorithm represents an advanced paradigm that integrates the strengths of FLC and ANN techniques, while addressing the inherent limitations of each approach [9,11]. The ANFIS algorithm adapts membership functions and fuzzy rules through an architecture comprising input and output layers, along with three intermediate layers that play an important role in calibrating the relationships between variables [24]. This structure enables the system to dynamically adjust the properties of the fuzzy representation [13,15]. For the ANFIS-MPPT strategy, the PV current ($I_{PV}$) and PV voltage ($V_{PV}$) serve as input variables, while the duty cycle (d) is generated as the output. The schematic representation of the ANFIS structure is shown in Fig. 2. The ANFIS algorithm defines its rules in the following form:

$$\begin{cases} \text{If } x\ A_1 \text{ and } y\ is\ B_1, \text{Then} : f_1 = p_1 x + q_1 y + r_1, \\ \text{If } x\ A_2 \text{ and } y\ is\ B_2, \text{Then} : f_2 = p_2 x + q_2 y + r_2. \end{cases} \quad (1)$$

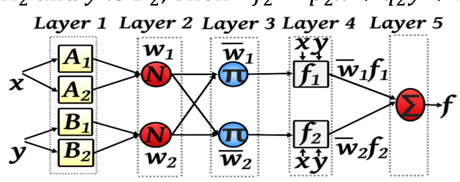


Fig. 2 – Descriptive architecture of the ANFIS strategy.

$A_1$, $A_2$, $B_1$, and $B_2$ define fuzzy sets corresponding to small, medium, and large operating time ranges. The variables $p_i$, $q_i$, and $r_i$ are the coefficients of the linear equation associated with layer i, where *x* and *y* are the input variables.

The first layer converts the digital inputs into fuzzy values using nodes that represent Gaussian membership functions. This information is tuned through a perturbation process, which more precisely determines the degree to which the inputs belong to each fuzzy set [9,10,24].

$$\begin{cases} O_{1,i} = \mu_{Ai}(x) \text{ for} : i = 1{,}2, \\ O_{1,i} = \mu_{Bi}(y) \text{ for} : i = 3{,}4, \end{cases} \quad (2)$$

where: $\mu_{Ai}(x)$ and $\mu_{Bi}(y)$ represent the membership function for inputs in the fuzzy sets $A_i$ and $B_i$, respectively.

The second layer functions as the ANFIS rule base, processing the fuzzy inputs produced by the first layer.

$$O_{2,i} = w_i = \mu_{Ai}(x)\mu_{Bi}(y)\ ; i = 1{,}2. \quad (3)$$

The third layer consists of fixed nodes that perform normalization by calculating the ratio of each rule's firing strength to the total firing strength of all bases.

$$O_{3,i} = \overline{w} = \frac{w_i}{w_1 + w_2}\ ; i = 1{,}2. \quad (4)$$

The fourth layer consists of adaptive nodes that perform the defuzzification process by generating a linear output for each rule.

$$O_{4,i} = \overline{w_i} f_i = \overline{w_i}(p_i x + q_i y + r_i), \quad (5)$$

where $f_i$ denotes the calculated output for each rule and $\overline{w_i}$ shows the firing strength of the normalized fire produced by layer *i*.

The fifth and final layer has one node that takes the linear outputs from the fourth layer and combines them to produce the system's final output.

$$O_{5,i} = \sum_i \overline{w_i}\, f_i = \frac{\sum_i w_i f_i}{\sum_i w_i}. \quad (6)$$

## 4. DYNAMIC MODELING OF THE APPLIED IM

The mathematically reduced model of the IM, illustrated in Fig. 3, is defined by the following equations [14,19,22]:

$$[\mathbf{L}]\frac{\mathrm{d}L[\mathbf{I}]}{dt} = [\mathbf{V}] - [\mathbf{R}][\mathbf{I}], \qquad [\mathbf{V}] = [V_{\mathrm{ds}} \quad V_{\mathrm{qs}}]^{\mathrm{T}}; [\mathbf{I}] = [I_{\mathrm{ds}} \quad I_{\mathrm{qs}} \quad I_{\mathrm{dr}} \quad I_{\mathrm{qr}} \quad I_{\mathrm{e}}]^{\mathrm{T}}, \tag{7}$$

where: [**V**], [**I**], [**L**] and [**R**] are the matrices showing the electrical variables of the IM, namely: the voltages, the currents, the inductances and the resistances, respectively.

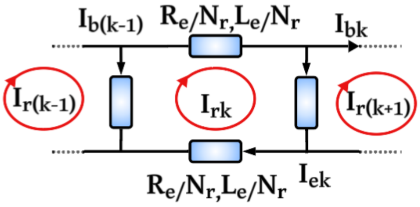


Fig. 3 – Rotor equivalent circuit of the applied IM.

$$[\boldsymbol{L}] = \begin{bmatrix} L_{sc} & 0 & -\frac{N_r}{2}M_{sr} & 0 & 0 \\ 0 & L_{sc} & 0 & -\frac{N_r}{2}M_{sr} & 0 \\ -\frac{3}{2}M_{sr} & 0 & L_{rc} & 0 & 0 \\ 0 & -\frac{3}{2}M_{sr} & 0 & L_{rc} & 0 \\ 0 & 0 & 0 & 0 & L_e \end{bmatrix}, \tag{8}$$

$$[\boldsymbol{R}] = \begin{bmatrix} R_{\mathrm{s}} & -L_{\mathrm{sc}}\omega & 0 & \frac{N_{\mathrm{r}}}{2}M_{\mathrm{sr}}\omega & 0 \\ L_{\mathrm{sc}}\omega & R_{\mathrm{s}} & -\frac{N_{\mathrm{r}}}{2}M_{\mathrm{sr}}\omega & 0 & 0 \\ 0 & 0 & [R_{\mathrm{rdd}} & R_{\mathrm{rdq}}] & 0 \\ 0 & 0 & [R_{\mathrm{rqd}} & R_{\mathrm{rqq}}] & 0 \\ 0 & 0 & 0 & 0 & R_{\mathrm{e}} \end{bmatrix}, \tag{9}$$

The electrical angle $\left(\left(= \alpha = p\frac{2\pi}{N_{\mathrm{r}}}\right)\right.$ is used to determine the total cyclic inductance of the stator and rotor phase ($L_{\mathrm{sc}}$, $L_{\mathrm{rc}}$). The following equations are used to identify these variables:

$$\begin{cases} L_{\mathrm{rc}} = L_{\mathrm{rp}} - M_{\mathrm{rr}} + \dfrac{2L_{\mathrm{e}}}{N_r} + 2L_{\mathrm{e}}(1-\cos(\alpha)), \\ L_{\mathrm{sc}} = \dfrac{6\mu_0 N_s^2 RL}{e\pi p^2} + L_{\mathrm{sf}}. \end{cases} \tag{10}$$

The cyclic inductance of the rotor, as well as the two mutual inductances of the stator/rotor and of the non-adjacent rotor meshes ($L_{\mathrm{rp}}$), ($M_{\mathrm{rr}}$), and ($M_{\mathrm{sr}}$), respectively, are calculated using the following system of equations:

$$\begin{cases} L_{\mathrm{rp}} = \dfrac{N_{\mathrm{r}}-1}{N_r^2}\dfrac{2\pi\mu_0}{\mathrm{e}}RL, \\ M_{\mathrm{rr}} = -\dfrac{1}{N_r^2}\dfrac{2\pi\mu_0}{\mathrm{e}}RL, \\ M_{\mathrm{sr}} = \dfrac{4\mu_0 N_s RL}{\pi e p^2}\sin\left(\dfrac{\alpha}{2}\right), \end{cases} \tag{11}$$

where $\mu_0$ is the air magnetic permeability and e represents the airgap.

The resistance sub-matrix serves as a reliable indicator of rotor faults, exhibiting unequal values that distinguish a faulty rotor from a healthy one. Here, $R_{\mathrm{bfk}}$ represents the resistance of the broken bar, and k denotes the index of the broken bar.

$$\begin{cases} R_{\mathrm{rdd,rqq}} = 2R_{\mathrm{b}}(1-\cos(\alpha)) + 2\dfrac{R_{\mathrm{e}}}{N_{\mathrm{r}}} + \dfrac{2}{N_{\mathrm{r}}}(1-\cos(\alpha)), \\ \qquad \sum\limits_k R_{\mathrm{bfk}}(1 \pm \cos((2k-1)\alpha)), \\ R_{\mathrm{rdq,rqd}} = -\dfrac{2}{N_r}(1-\cos(\alpha))\sum\limits_k R_{\mathrm{bfk}}\sin((2k-1)\alpha). \end{cases} \tag{12}$$

The following equation represents the final torque formula derived from the reduced IM model:

$$C_{\mathrm{e}} = \frac{3}{2}p\frac{N_{\mathrm{r}}}{2}M_{\mathrm{sr}}(I_{\mathrm{ds}}I_{\mathrm{qr}} - I_{\mathrm{qs}}I_{\mathrm{dr}}). \tag{13}$$

## 5. DTC STRATEGY OF THE INVESTIGATED SWPS

The DTC strategy applied in the SWPS ensures reliable and efficient control of the IM under both healthy and faulty operating conditions. It mostly focuses on regulating electromagnetic torque and stator flux through mathematical models based on stator current and voltage measurements of the IM. The three-phase voltage source inverter (VSI) supplying the induction motor is controlled using a switching table, as shown in Table 1. This table takes three inputs: the stator flux position ($S_i$), the torque correction error ($\Delta T_{\mathrm{em}}$), and the flux correction error ($\Delta\varphi$). Based on these inputs, the table determines the appropriate switching states ($S_a$, $S_b$, and $S_c$) that control the inverter feeding the IM. The key equations governing the DTC strategy are as follows [8,18,21]:

$$\begin{cases} \varphi_{s\alpha} = \displaystyle\int_0^t (V_{s\alpha} - R_s I_{s\alpha})\mathrm{d}t\,, \\ \varphi_{s\beta} = \displaystyle\int_0^t (V_{s\beta} - R_s I_{s\beta})\mathrm{d}t\,, \end{cases} \tag{14}$$

$$\varphi_s = \sqrt{\varphi_{s\alpha}^2 + \varphi_{s\beta}^2}\,; \theta_s = \tan^{-1}\left(\frac{\varphi_{s\alpha}}{\varphi_{s\beta}}\right), \tag{15}$$

where $\varphi_s$ is the stator flux magnitude and $\theta_s$ represents the stator flux angle.

The electromagnetic torque in the stationary reference frame ($\alpha$,$\beta$) is given by,

$$T_{em} = \frac{3}{2}p(\varphi_{s\alpha}I_{s\beta} - \varphi_{s\beta}I_{s\alpha}). \tag{16}$$

*Table 1*

Applied the switching table in the classical DTC strategy.

| $\Delta\varphi_s$ | $\Delta T_{em}$ | $S_i$ | | | | | |
|---|---|---|---|---|---|---|---|
| | | $S_1$ | $S_2$ | $S_3$ | $S_4$ | $S_5$ | $S_6$ |
| 1 | 1 | $V_2$ | $V_3$ | $V_4$ | $V_5$ | $V_6$ | $V_1$ |
| | 0 | $V_7$ | $V_0$ | $V_7$ | $V_0$ | $V_7$ | $V_0$ |
| | -1 | $V_6$ | $V_1$ | $V_2$ | $V_3$ | $V_4$ | $V_5$ |
| 0 | 1 | $V_3$ | $V_4$ | $V_5$ | $V_6$ | $V_1$ | $V_2$ |
| | 0 | $V_0$ | $V_7$ | $V_0$ | $V_7$ | $V_0$ | $V_7$ |
| | -1 | $V_5$ | $V_6$ | $V_1$ | $V_2$ | $V_3$ | $V_4$ |

The DTC strategy enables motor speed control using a standard PI controller, which sets and maintains the reference torque at an appropriate level [1]. The reference speed ($\Omega_{\mathrm{rref}}$) in the investigated SWPS is determined by the difference between the two speeds $\Omega_1$ and $\Omega_2$ [5].

$$\Omega_{\mathrm{rref}} = \Omega_1 - \Omega_2, \tag{17}$$

The first speed ($\Omega_1$) is calculated based on the power generated by the PV array, taking into account changes in irradiance. The formula for this speed is as follows:

$$\Omega_{\text{rref}} = \sqrt[3]{\frac{P_{\text{PV}}}{K_{\text{p}}}}, \tag{18}$$

where: $K_p$ is the centrifugal pump constant.

The second speed ($\Omega_2$) is controlled using a standard PI controller. The regulator's input is the voltage error resulting from the comparison between the reference value ($V_{dcref}$) and the measured value ($V_{dcmes}$). Furthermore, the same applied regulator is used to keep the DC bus voltage constant at its reference value.

$$\begin{cases} \Omega_2 = \Omega_2(n-1) + K_{\text{Pdc}}\big(\Delta V_{\text{dc}}(n) - \Delta V_{\text{dc}}(n-1)\big) \\ \qquad + K_{\text{Idc}}\Delta V_{\text{dc}}(n), \\ \Delta V_{\text{dc}} = V_{\text{dcref}} - V_{dcmes}, \end{cases} \tag{19}$$

where: $\Omega_2(n-1)$ denotes the previous value of $\Omega_2$, $K_{Pdc}$ and $K_{Idc}$ represent, respectively, the proportional and integral parameters of the PI regulator.

The developed SWPS uses a centrifugal pump coupled with the IM that can operate reliably under all conditions and with varying levels of irrigation water demand, even in faulty states. The power of a hydraulic pump can be calculated using the following formula [25]:

$$P_{\text{m}} = \frac{\rho g H Q_p}{\eta_p}, \tag{20}$$

where: $Q_p$ is the pump's flow; g represents gravitational acceleration; H is the entire dynamic head; ρ denotes the water density, and $\eta_p$ is the pump efficiency.

The pump constant, denoted $K_p$, representing the quotient of the power ($P_m$) divided by the cube of the measured rotor speed ($\Omega_{rmes}$) can be calculated as [1]:

$$K_{\text{p}} = \frac{P_m}{\Omega_{\text{rmes}}^3}. \tag{21}$$

In this paper, the FFT technique is utilized for closed-loop monitoring and diagnosis of the IM condition in the SWPS (healthy or faulty state). The transformation from the time domain to the frequency domain via the FFT technique is defined by the following equation [23]:

$$K_{\text{s}}(f) = \int_{-\infty}^{+\infty} K_{\text{s}}(t)\, e^{-\text{j}2\pi f t} \text{d}t, \tag{22}$$

where j, $f$, $K_s(f)$ and $k_s(t)$ represent, respectively, the unitary imaginary number, the frequency, the signal in the frequency domain and the original signal in the time domain.

## 6. EXPERIMENTAL RESULTS

As illustrated in Fig. 4, the OPAL-RT5600 platform was adopted to evaluate and validate the performance of the investigated SWPS under realistic conditions, encompassing a variety of operating scenarios. The specifications of the solar panel, the IM with DTC strategy, and the centrifugal pump incorporated in the investigated SWPS are comprehensively detailed in Appendix Table 3.

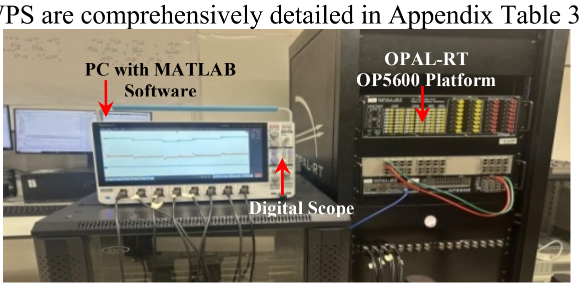


Fig. 4 – Real-time implementation: setup of the studied SWPS.

During the HIL tests, the irradiation profile consisted of four distinct levels: 900 W/m², 500 W/m², 700 W/m², and 1000 W/m². The experimental waveforms recorded by the digital oscilloscope are depicted in Figs. 5 to 9.

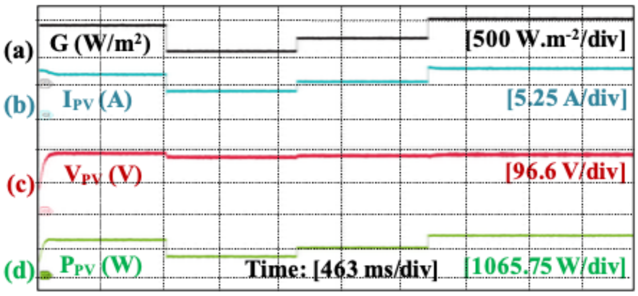


Fig. 5 – Experimental results: (a) Variable solar irradiation profile; (b) PV current; (c) PV voltage; and (d) PV power.

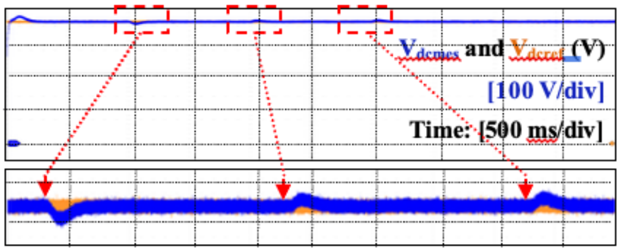


Fig. 6 – Experimental result: DC output voltage with its desired value.

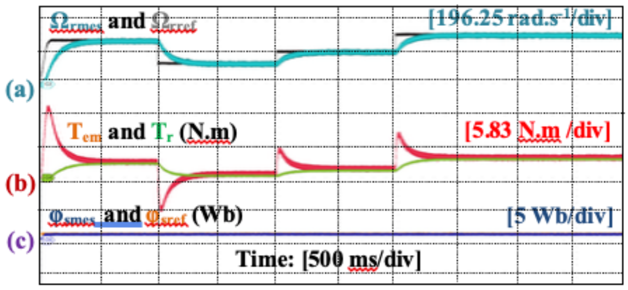


Fig. 7 – Experimental results: (a) Motor speed ($\Omega_r$); (b) Electromagnetic and load torque; and (c) Stator flux.

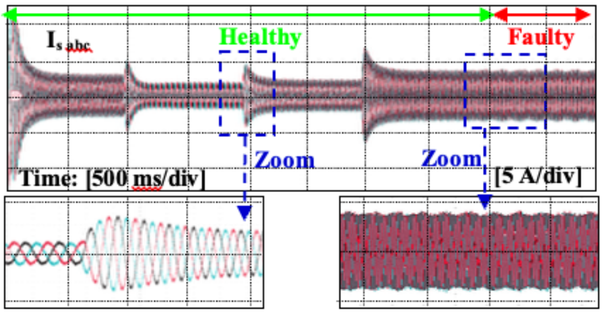


Fig. 8 – Experimental result: Stator currents of the investigated SWPS under healthy and faulty IM conditions.

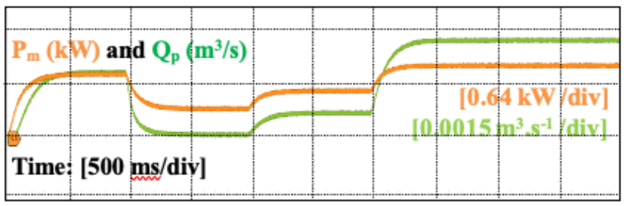


Fig. 9 – Experimental results: Hydraulic power ($P_m$) and pump flow rate ($Q_P$) of the investigated SWPS.

As presented in Fig. 5, variations in solar irradiance lead to corresponding changes in the PV panel's current and power, while the PV voltage remains approximately constant. According to Figs. 6 and 7, the investigated SWPS demonstrates high efficiency in real-time monitoring and control, accurately tracking the reference values of DC bus voltage, rotational speed, electromagnetic torque, and stator flux. The DTC strategy enables the induction motor in the SWPS to maintain apparently normal operation, effectively masking the presence of two broken rotor bars (TBRB), as key indicators such as speed, torque, and flux show no signs of the fault. Under normal operating conditions, the stator currents in Fig. 8 exhibit a pure sinusoidal waveform. In contrast, during IM faults, noticeable fluctuations in current amplitude are observed, clearly indicating the presence of a fault. Thus, applying FFT analysis is essential to detect and confirm the presence of the fault. Moreover, the stator currents respond appropriately to sudden variations caused by changes in solar irradiance, both under healthy and faulty SWPS operating conditions. According to Fig. 9, the pump's hydraulic power responds promptly to variations in water flow, even at low levels. Finally, under standard test conditions, the SWPS consistently maintains an irrigation flow rate of approximately 3 l/s, regardless of whether the IM is operating under healthy or faulty conditions.

The application of the FFT to stator current signals constitutes an effective diagnostic approach for identifying faults in electrical machines [23]. In a healthy state, the current waveform is regular and follows the fundamental frequency with minimal distortion. At fault, the current characteristics change to exhibit frequency bands around the fundamental frequency that reflect the presence and type of the fault [14]. Fig. 10 illustrates the FFT analysis of the IM's first-phase stator current within the SWPS, highlighting the differences between healthy and faulty operating conditions of the IM. The magnitude of the applied faults increases according to the number of affected rotor bars [20].

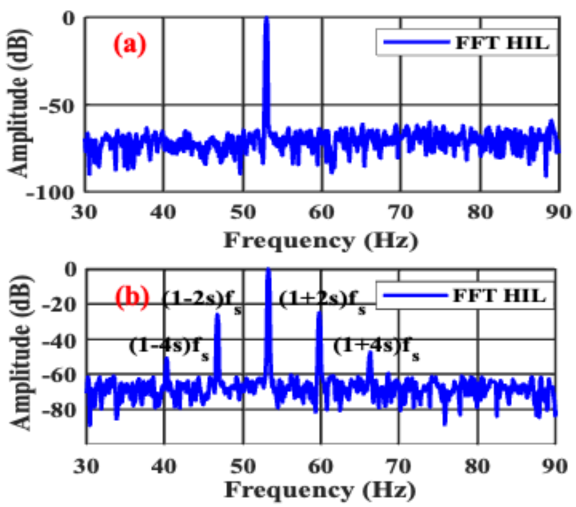


Fig. 10 – FFT analysis of the first stator current phase under (a) healthy and (b) faulty IM operating conditions.

Table 2 shows the additional harmonics $(f_s \pm 2sf_r)$ $(f_s \pm 4sf_r)$, where $f_s$ denotes the main supply frequency, $f_r$ represents the motor rotation frequency, and s is the slip of the IM. The inferred frequencies show high agreement with the calculated frequencies, with almost no differences across the various operating points studied, validating the model. Furthermore, this study assesses the total harmonic distortion (THD) of the stator current under the DTC strategy of the IM incorporated in the SWPS. As illustrated in Fig. 11, the healthy operating condition yields a reduced THD of 7.64% (Fig. 11(a)), whereas a fault results in a notable increase in distortion, with the THD rising to 11.26% (Fig. 11(b)).

*Table 2*

Frequency analysis using the FFT technique.

| | $(1-4s)f_s$ | $(1-2s)f_s$ | $(1+2s)f_s$ | $(1+4s)f_s$ |
|---|---|---|---|---|
| Motor with TBRB | $s_{HIL} = 0.0612$ | | | |
| $f_{Deduced\ HIL}$ (Hz) | 40.2 | 46.7 | 59.78 | 66.3 |
| $f_{Calculated}$ (Hz) | 40.2255 | 46.7353 | 59.7842 | 66.3038 |
| Amplitude $_{HIL}$ (dB) | -50.77 | -25.9 | -24.81 | -47.31 |

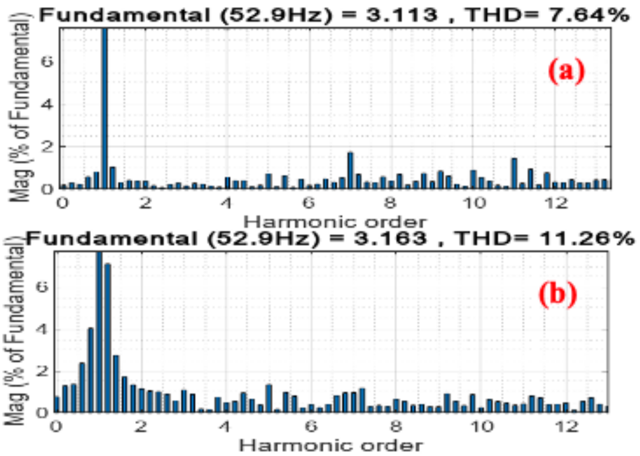


Fig. 11 –THD evaluation of the first stator current phase under (a) healthy and (b) faulty IM operating conditions

## 7. CONCLUSIONS

This paper presents a high-performance control system that has been developed for use with a SWPS. The investigated system is designed to improve the efficiency and sustainability of agricultural irrigation. It overcomes the limitations of conventional technologies by integrating ANFIS and DTC strategies to ensure more efficient and reliable operation. The ANFIS algorithm employs a training mechanism that enables real-time adaptation to varying operating conditions without the need for predefined mathematical models. This enhances MPPT performance beyond that of traditional techniques. Moreover, it allows for accurate adjustment of the reference speed based on solar irradiance data. The DTC method is used to regulate the motor driving the centrifugal pump. This ensures efficient and stable operation of the SWPS. Furthermore, the proposed diagnostic device utilizes a simple yet effective FFT analysis of stator currents to reliably detect the broken rotor bars in the IM. This method facilitates real-time monitoring of the motor's condition, enabling prompt maintenance interventions that help ensure the continuous and efficient operation of the solar pumping system. Finally, the effectiveness of the investigated SWPS has been rigorously validated through HIL testing using the OPAL-RT platform.

## CREDIT AUTHORSHIP CONTRIBUTION

NORA REZAIGUIA: Methodology, simulation, visualization, writing, review.

OUALID AISSA: Supervision, methodology, writing, review.

HICHAM TALHAOUI: Software, methodology, investigation, review.
ABDELBASSET KRAMA: HIL implementation, validation, and data analysis.
ABDELHALIM KESSAL: Supervision, methodology, writing, review.
ABDERRAHIM REFFAS: Conceptualization, writing, review.

## APPENDIX

*Table 3*
Specifications of the investigated SWPS.

| Solar panel parameters | Numerical values |
|---|---|
| Peak solar power ($P_{mpp}$) | 213.15 W |
| Cells within each module ($N_{cell}$) | 60 |
| Maximum voltage ($V_{mpp}$) | 29 V |
| Open circuit voltage ($V_{oc}$) | 36.3 V |
| Maximum current ($I_{mpp}$) | 7.35 A |
| Temperature coefficient of $V_{oc}$ | -0.36099 % / °C |
| Temperature coefficient of $I_{sc}$ | 0.102 % / °C |
| **IM parameters** | **Numerical values** |
| Rated power ($P_n$) | 1.1 kW |
| Nominal voltage of the stator ($V_n$) | 220 V |
| Nominal load current ($I_n$) | 4.6 A |
| Number of pole pairs (p) | 1 |
| Resistance of the stator phase ($R_s$) | 7.58 Ω |
| Resistance of the rotor bars ($R_b$) | 150 μΩ |
| Resistance of end ring segment ($R_e$) | 150 μΩ |
| Inductance of the rotor bars ($L_b$) | 0.1 μH |
| Inductance of end ring ($L_e$) | 0.1 μH |
| Stator leakage inductance ($L_{sf}$) | 26.5 mH |
| Number of turns per stator phase ($N_s$) | 160 |
| Number of rotor bars ($N_r$) | 16 |
| Length of the rotor (l) | 65 mm |
| Airgap (e) | 0.2 mm |
| Inertia moment (J) | 0.0054 kg m$^2$ |
| Median air gap radius (R) | 35.76 mm |
| **DTC parameters** | **Numerical values** |
| Torque hysteresis bandwidths ($\Delta T_{em}$) | 0.65 Nm |
| Flux hysteresis bandwidths ($\Delta\varphi_s$) | 0.01 Wb |
| Switching frequency ($f_{sw}$) | 10 kHz |
| DC bus voltage ($V_{dc}$) | 520 V |
| **Centrifugal pump parameters** | **Numerical values** |
| Pump's flow ($Q_p$) | 0.0027 m$^3$/s |
| Dynamic head (H) | 28 m |
| Pump efficiency ($\eta_p$) | 0.8 |

*Received on 23 September 2025*

## REFERENCES

1. S. Murshid, B. Singh, “Implementation of PMSM drive for a solar water pumping system”, IEEE Transactions on Industry Applications, **55**, *5*, pp. 4956–4964 (2019).
2. K. Venugopalan, J. Varghese, J. Thankaswamy, “African vulture optimized integrated control technique for PV-fed open-end winding induction motor pump application”, Rev. Roum. Sci. Techn. – Électrotechn. et Énerg., **69**, *1*, pp. 27–32 (2024).
3. B.P. Rachaputi, J.R. Louis, M. Sridharan, “Solar photovoltaic array fed single-stage sensorless vector control of induction motor drive for water pumping applications”, International Journal of Energy and Environmental Engineering, **14**, *4*, pp. 643–660 (2023).
4. L. Khettache, M.R. Rezoug, A. Saadi, L. Sahraoui, “A novel design of a photovoltaic system based on a linear induction motor and reciprocating pump”, Rev. Roum. Sci. Techn. – Électrotechn. et Énerg., **70**, *1*, pp. 3–8 (2025).
5. I. Saady, M. Karim, B. Bossoufi, N. El Ouanjli, S. Motahhir, B. Majout, “Optimization and control of photovoltaic water pumping system using Kalman filter-based MPPT and multilevel inverter-fed DTC-IM”, Results in Engineering, **17**, p. 100829 (2023).
6. M. Kumar, K.P. Panda, J.C. Rosas-Caro, A. Valderrabano-Gonzalez, G. Panda, “Comprehensive review of conventional and emerging maximum power point tracking algorithms for uniformly and partially shaded solar photovoltaic systems”, IEEE Access, **11**, pp. 31778–31812 (2023).
7. M.I. Abdelwanis, A.A. Zaky, “Maximum power point tracking in a perovskite solar pumping system with a six-phase induction motor”, Rev. Roum. Sci. Techn. – Électrotechn. et Énerg., **69**, *1*, pp. 15–20 (2024).
8. O. Aissa, A. Reffas, A. Krama, R. Benkercha, H. Talhaoui, H. Abu-Rub, “Advanced direct torque control based on neural tree controllers for induction motor drives”, ISA Transactions, **148**, pp. 92–104 (2024).
9. X. Wu, N. Furukawa, H. Tao, H. Farajian, “An efficient tracking of MPP in PV systems using hybrid HCS-PS algorithm based ANFIS under partially shaded conditions”, Soft Computing, **26**, *12*, pp. 5699–5717 (2022).
10. M. Mehta, B. Mehta, “Control strategies for grid-connected hybrid renewable energy systems: Integrating modified direct torque control based doubly fed induction generator and ANFIS based maximum power point tracking for solar PV generation”, e-Prime – Advances in Electrical Engineering, Electronics and Energy, **8**, p. 100575 (2024).
11. E. Bouchetob, B. Nadji, “Deep learning and WBG devices combining to improve PV system efficiency: ANFIS-based MPPT controller”, Rev. Roum. Sci. Techn. – Électrotechn. et Énerg., **70**, *4*, pp. 453–458 (2025).
12. B. Babes, F. Albalawi, N. Hamouda, S. Kahla, S.S.M. Ghoneim, “Fractional-fuzzy PID control approach of photovoltaic-wire feeder system (PV-WFS): Simulation and HIL-based experimental investigation”, IEEE Access, **9**, pp. 159933–159954 (2021).
13. M. Hassan, M.A. Elseify, M. K.F. Ahmed, N.V. Korovkin, A. Refaat, “Highly efficient MPP tracker based on adaptive neuro-fuzzy inference system for stand-alone photovoltaic generator system”, International Journal of Renewable Energy Research, **12**, *1*, pp. 209–217 (2022).
14. O. Aissa, A. Reffas, H. Talhaoui, D. Ziane, A. Saim, “An improved direct torque control with an advanced broken-bar fault diagnosis for induction motor drives”, International Transactions on Electrical Energy Systems, **2023**, *1*, p. 8816896 (2023).
15. K. Xia, Y. Li, B. Zhu, “Improved photovoltaic MPPT algorithm based on ant colony optimization and fuzzy logic under conditions of partial shading”, IEEE Access, **12**, pp. 44817–44825 (2024).
16. O. Aissa, R. Benkercha, Z. Bouchama, B. Babes, I. Colak, “Experimental assessment of fuzzy-tree adaptive synergetic control law for DC/DC buck converter”, Soft Computing, **28**, *20*, pp. 12191–12205 (2024).
17. I. Saady, B. Majout, I. El Kafazi, M. Karim, B. Bossoufi, N. El Ouanjli, S. Mahfoud, A. Althobaiti, T.A.H. Alghamdi, M. Alenezi, “Improving photovoltaic water pumping system performance with ANN-based direct torque control using real-time simulation”, Scientific Reports, **15**, *1*, p. 4024 (2025).
18. R. Belal, M. Flitti, M.L. Zegai, “Tuning of PI speed controller in direct torque control of dual star induction motor based on genetic algorithms and neuro-fuzzy schemes”, Rev. Roum. Sci. Techn. – Électrotechn. et Énerg., **69**, *1*, pp. 9–14 (2024).
19. R. Sarkar, J. Retna Kumar, R. Sridhar, S. Vidyasagar, “A new hybrid BAT-ANFIS-based power tracking technique for partial shaded photovoltaic systems”, International Journal of Fuzzy Systems, **23**, *5*, pp. 1313–1325 (2021).
20. H. Talhaoui, T. Ameid, A. Kessal, “Energy eigenvalues and neural network analysis for broken bars fault diagnosis in induction machine under variable load: experimental study”, Journal of Ambient Intelligence and Humanized Computing, **13**, *5*, pp. 2651–2665 (2022).
21. S. Gdaim, A. Mtibaa, M.F. Mimouni, “Artificial neural network-based DTC of an induction machine with experimental implementation on FPGA”, Engineering Applications of Artificial Intelligence, **121**, p. 105972 (2023).
22. R. Senthil Kumar, I. Gerald Christopher Raj, I. Alhamrouni, S. Saravanan, N. Prabaharan, S. Ishwarya, M. Gokdag, M. Salem, “A combined HT and ANN-based early broken bar fault diagnosis approach for IFOC-fed induction motor drive”, Alexandria Engineering Journal, **66**, pp. 15–30 (2023).
23. H. Talhaoui, T. Ameid, O. Aissa, A. Kessal, “Wavelet packet and fuzzy logic theory for automatic fault detection in induction motor”, Soft Computing, **26**, *21*, pp. 11935–11949 (2022).
24. Z. Alaas, G.E.A. Eltayeb, M. Al-Dhaifallah, M. Latifi, “A new MPPT design using PV-BES system using modified sparrow search algorithm based ANFIS under partially shaded conditions”, Neural Computing and Applications, **35**, *19*, pp. 14109–14128 (2023).
25. Z. Ben Safia, M. Allouche, M. Chaabane, “Renewable energy management of a hybrid water pumping system (photovoltaic/wind/battery) based on Takagi–Sugeno fuzzy model”, Optimal Control Applications and Methods, **44**, *2*, pp. 373–390 (2023).